Diamond & Related Materials 165 (2026) 113690

Contents lists available at ScienceDirect

Diamond & Related Materials

journal homepage: www.elsevier.com/locate/diamond

Ultrafast electron cooling in $Ti_3C_2T_x$ MXene revealed by time-resolved photoemission spectroscopy

Jurij Urbančič [a,*], Fyodor Malchik [b], Kaiyrgali Zhumadil [b], Gian Marco Pierantozzi [c], Monika Schied [c], Sara Dottorini [c], Riccardo Cucini [c], Pietro Parisse [c], Giorgio Rossi [c,d], Rokaya Osama [a], Lakshmi Rajan [a], Egon Pavlica [a], Barbara Ressel [a]

[a] University of Nova Gorica, Vipavska 13, Nova Gorica, 5000, Slovenia
[b] al-Farabi Kazakh National University, Faculty of Chemistry and Chemical Technology, Almaty, Kazakhstan
[c] CNR-Istituto Officina dei Materiali, Unità di Trieste, Strada Statale 14, km 163.5, 34149, Basovizza, TS, Italy
[d] Dipartimento di Fisica, Università degli Studi di Milano, Via Celoria 16, 20133, Milano, Italy

ARTICLE INFO

Keywords:
$Ti_3C_2T_x$
MXene
High-harmonic generation
HHG
Time-resolved
Photoelectron spectroscopy

ABSTRACT

Ultrafast electron dynamics in a $Ti_3C_2T_x$ MXene thin film (where T_x denotes surface terminations) were investigated using time-resolved photoemission spectroscopy with temporal resolution of 110 fs. Near-infrared optical excitation at 800 nm induces a transient redistribution of electronic states in the vicinity of the Fermi level, which is directly probed using extreme-ultraviolet (26.5 eV) pulses. The measured signal reveals a rapid modification of the electronic distribution immediately after excitation, followed by relaxation on sub-0.5 ps timescales, as quantified by the evolution of the electronic temperature. These results provide direct insight into hot-electron lifetimes and open the study of relaxation pathways in MXene thin films, establishing a framework for further understanding and optimizing their performance.

1. Introduction

Femtosecond time-resolved photoelectron spectroscopy (tr-PES) has emerged as a powerful tool for probing electron dynamics in solids, providing direct access to the fundamental interactions that govern energy redistribution on ultrafast timescales [1–6]. In this technique, an optical pump pulse excites the system out of equilibrium, followed by a time-delayed probe pulse that photoemits electrons and maps the transient electronic structure. Using extreme-ultraviolet (XUV) from the high-harmonic-generation (HHG) process [7,8] as probe can overcome the limitations of visible and ultraviolet light from traditional laser sources [9,10]. This provides access to a broader range of energy and momentum space below the Fermi level. Through this nonlinear process, intense femtosecond laser pulses are focused into a noble gas, generating coherent radiation at odd integer multiples of the driving laser frequency, reaching even soft x-rays [11–13]. This expanded phase space has made HHG-based tr-PES a key method for investigating nonequilibrium electronic structure in emerging quantum materials [14]. In particular, it has enabled direct tracking of ultrafast spectral-weight redistribution, gap dynamics and the collapse or recovery of collective order in charge-density-wave [15,16] and superconducting systems [17,18].

Beyond the bulk systems, this method has also proven to be particularly powerful in the investigation of two-dimensional (2D) materials. Graphene, serving as a benchmark, has been studied to directly resolve hot-carrier thermalization and subsequent cooling through electron-phonon coupling [19,20]. Motivated by these advances, attention has been turned to $Ti_3C_2T_x$ (where T_x denotes surface termination groups depending on the synthesis and delamination procedures [21]), the first [22] and most extensively studied member of emerging 2D materials called MXenes [23,24]. Recent advances in synthesis and thin-film fabrication have led to its electrical conductivities exceeding 24×10^3 S/cm [25], making $Ti_3C_2T_x$ one of the most conductive solution-processed materials reported to date. In addition, the investigation of its charge carrier mobility demonstrated the highest experimentally measured charge-carrier mobility in MXene thin films, reaching values of up to 279 cm^2/Vs [26]. However, despite this rapid progress in macroscopic transport performance, direct experimental constraints on the ultrafast, microscopic charge-carrier relaxation pathways in MXene thin films remain limited. As a result, the underlying hot-carrier

* Corresponding author.
E-mail address: jurij.urbancic@ung.si (J. Urbančič).

https://doi.org/10.1016/j.diamond.2026.113690
Received 24 February 2026; Received in revised form 7 April 2026; Accepted 29 April 2026
Available online 30 April 2026

dynamics are not yet fully understood.

While previous time-resolved studies of MXenes have relied primarily on optical pump–probe methods [27–31], this work, to the best of our knowledge, presents the first tr-PES measurements on $Ti_3C_2T_x$. By employing the HHG-generated XUV probe at 26.5 eV, we report the femtosecond nonequilibrium electronic response of the MXene thin films following optical excitation with an 800 nm pump beam. Analysing pump-induced changes in the photoemission lineshape in the vicinity of the Fermi edge, we extract the time-dependent electronic temperature increase and subsequent cooling. This relaxation dynamics is characterized by a decay time of 138 fs, reflecting rapid energy dissipation of photoexcited carriers via an efficient scattering with optical phonons. Such rapid thermalization is expected to favour photothermal and bolometric responses, while posing a challenge for device concepts that require long-lived hot carriers.

2. Experimental part

2.1. MXene synthesis and sample preparation

To obtain an aqueous suspension of delaminated $Ti_3C_2T_x$ flakes, the Ti_3AlC_2 MAX phase was selectively etched and subsequently delaminated. In a typical procedure, 1.6 g of LiF was dissolved in 20 ml of concentrated hydrochloric acid under constant stirring in a plastic container. After complete dissolution, 1 g of Ti_3AlC_2 was slowly added in small portions to avoid rapid hydrogen evolution. The mixture was stirred for 48 h at 35 °C on a sand bath.

The resulting suspension was washed repeatedly with distilled water by centrifugation (3500 rpm, 5 min) until the supernatant reached a pH of approximately 5.0–5.5, thereby removing residual aluminium-containing species. The washed material was then subjected to ultrasonication (5 min, 100% power) to promote delamination, followed by centrifugation (3500 rpm, 5 min) to separate delaminated flakes from non-exfoliated particles. The concentration of the resulting aqueous MXene suspension was determined by vacuum filtration and was found to be approximately 10 mg/ml.

For thin-film deposition, the aqueous $Ti_3C_2T_x$ suspension was diluted in methanol to a final concentration of 0.5 mg/ml. The use of methanol as a solvent facilitates spray coating by reducing surface tension and enhancing solvent evaporation during deposition. The MXene film was deposited onto Si substrates with a 230 nm thick SiO2 layer using a spray-coating technique with a micro-compressor-assisted spray gun. Prior to deposition, the substrates were sonicated in acetone and dried under an argon flow. During the coating process, the substrates were maintained at 80 °C, and the deposition time was fixed at 15 s, resulting in films with a thickness of approximately 20 nm (see Supplementary Information).

As MXenes are known to degrade upon exposure to ambient conditions, even in the solid state [32,33], their exposure to air was minimized by sealing the samples in a transport container filled with nitrogen. The samples were exposed to the atmosphere only briefly during transfer into the experimental chamber.

2.2. Experimental setup for time-resolved photoemission spectroscopy

Time-resolved XUV photoemission spectroscopy measurements were performed at the NFFA-SPRINT laboratory [34,35], located at CNR-IOM (Trieste, Italy) within the NFFA infrastructure. The XUV probe pulses were generated via the HHG process driven by the Twin-PHAROS (Light Conversion) laser system operating at a fundamental wavelength of 1030 nm and a 50 kHz repetition rate. After frequency doubling, the shorter-wavelength output was used to drive the HHG process, which is particularly well suited for time-resolved photoemission spectroscopy due to its improved efficiency and temporal resolution [36]. A separate portion of the laser output was routed to an optical parametric amplifier (OPA) to generate the pump pulses used to excite the sample.

In the present experiment, the overall temporal resolution, determined from the pump-probe cross-correlation in other experiments with the same setup, was 110 fs (Gaussian FWHM). The sample was excited using 800 nm pump pulses with a fluence of 250 μJ/cm^2, while the photoemission was probed using 26.5 eV XUV pulses. Both pump and probe beams were p-polarized and focused to a spot diameter of approximately 250 μm and 100 μm respectively on the sample surface. All measurements were performed at room temperature under ultrahigh vacuum conditions, with a base pressure of about 1×10^{-10} mbar.

3. Results and discussion

3.1. Structural and surface characterization

X-ray diffraction (XRD) of the prepared film (Fig. 1a) exhibits a dominant (00*l*) reflection at $2\theta = 7.8°$ and a weaker feature at 16.25°, corresponding to (002) and (004) planes of stacked flakes, respectively. These peaks give interplanar spacings of 11.35 Å and 5.45 Å, consistent with previously reported diffraction signatures of MXenes [37–39]. The absence of additional sharp reflections suggests no detectable crystalline impurity phases (e.g., residual MAX) within the sensitivity of the measurement. The dominance of (00*l*) peaks indicates a strongly preferred orientation, consistent with flakes lying parallel to the substrate, while the presence of the (004) harmonic confirms a well-defined lamellar repeat spacing in the stacked film. Higher-order (00*l*) reflections are expected but are too weak to resolve, consistent with the thin-film geometry and peak broadening from limited stacking coherence and interlayer disorder.

Prior to the photoemission measurement, the sample was cleaned in situ by stepwise annealing under ultrahigh vacuum conditions. The annealing sequence consisted of heating to 100 °C for 45 min, followed by 350 °C for 10 min, and finally 500 °C for 10 min. This procedure was chosen to remove surface contamination in order to improve the quality of the static XUV photoemission spectrum. We note that this treatment can modify the relative population of surface terminations. Therefore, the tr-PES data reported below probe the annealed, in situ cleaned $Ti_3C_2T_x$ surface state rather than the as-prepared ambient-exposed film.

To assess the annealing procedure, X-ray photoelectron spectroscopy (XPS) was used to monitor the surface composition and termination chemistry of the MXene film before and after in situ cleaning (Fig. 1b). With reduced contamination, the Ti 2p appears stronger and sharper, while the lower C 1 s intensity is consistent with the removal of adventitious carbon. Changes in O 1 s suggest desorption of –OH surface terminations or their transformation into more stable =O terminations, while the F 1 s peak indicates fluorine terminations remain, although in smaller amounts since the initial signal is suppressed by the contamination [40,41]. In addition, the static XUV photoemission spectrum measured before and after annealing shows a substantially clearer Fermi edge after cleaning (Fig. S2, Supplementary information), which was the key requirement for the subsequent tr-PES analysis. Thus, the annealing was primarily motivated by the need to obtain a sufficiently clean and well-defined electronic spectrum for pump-probe measurements.

3.2. Ultrafast electronic response

In Fig. 2 we summarize the photoemission response of the $Ti_3C_2T_x$ MXene thin film under femtosecond optical excitation at 800 nm. Fig. 2a shows the static photoemission spectrum recorded in the absence of the pump pulse, featuring a well-defined Fermi edge plotted on an energy axis referenced to the Fermi level ($E - E_F = 0$) and no band gap at the Fermi level, consistent with the metallic character of the $Ti_3C_2T_x$ [42–44]. To explore how this electronic structure evolves following optical excitation, Fig. 2b presents the photoemission intensity map recorded over the same energy window as Fig. 2a, plotted as a function of the pump-probe delay. This two-dimensional map reveals the temporal evolution of the photoemission signal across the E_F, showing a

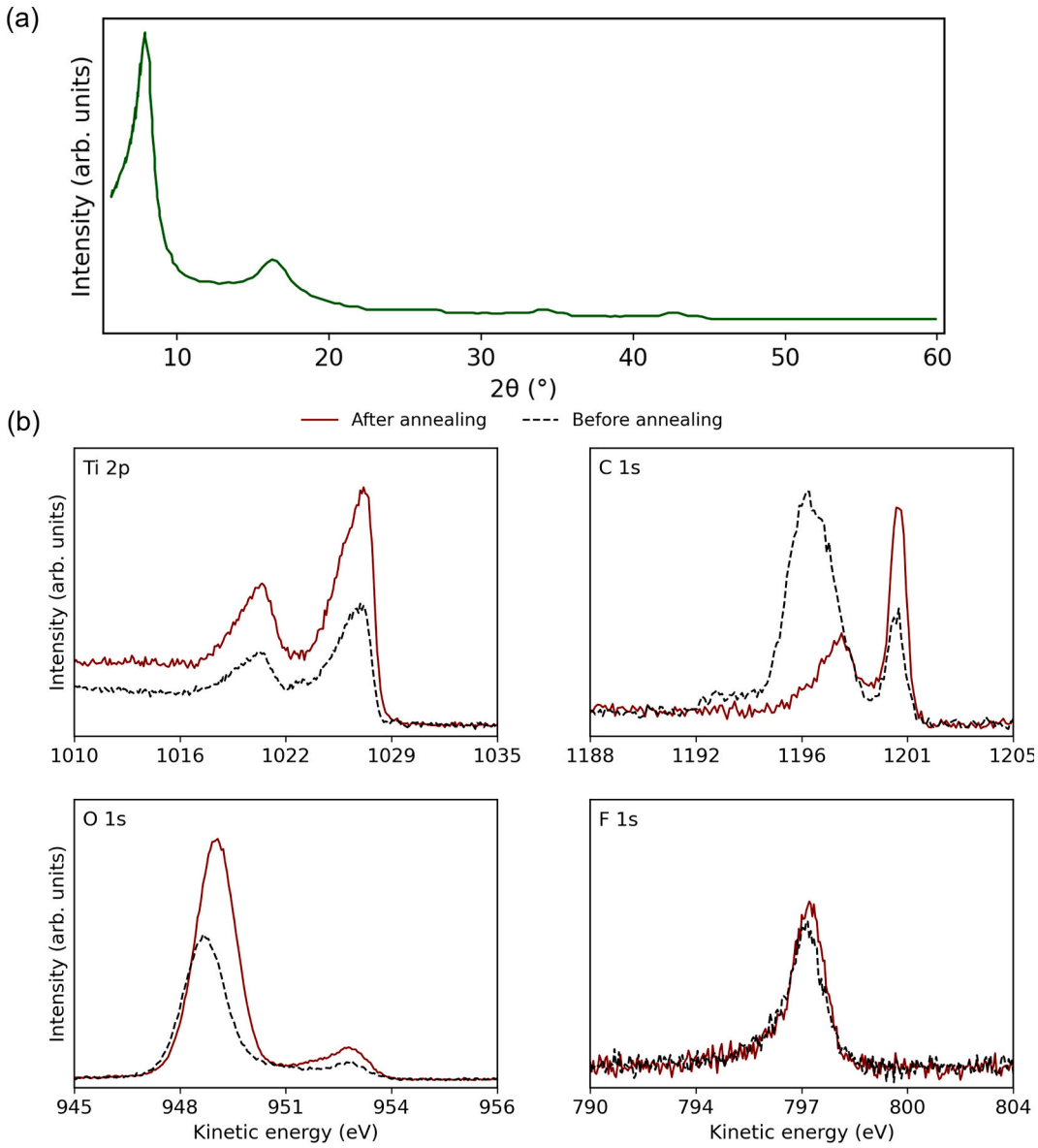

Fig. 1. (a) XRD spectra of the $Ti_3C_2T_x$ thin film. The main reflection at $2\theta = 7.8^\circ$ corresponds to an interlayer spacing of 11.35 Å, while the weaker feature near 16.25° (≈ 5.45 Å). (b) Effect of the annealing on the XPS spectrum at various elemental peaks. The improvement of the peak shape and intensity is due to the removal of contaminants, mainly carbon and water.

redistribution of spectral weight immediately after excitation.

To isolate the pump-induced response from the static background, the equilibrium spectrum recorded at negative delay was subtracted from the time-resolved data, yielding the differential photoemission map shown in Fig. 2c. The differential map was obtained by subtracting the average spectrum at negative delays. Therefore, the pre-pump signal is zero only on average, while the remaining weak fluctuations reflect statistical noise. This representation enhances the transient response, revealing a pronounced positive signal above the Fermi level (filling of states) accompanied by a corresponding negative signal below it (depletion of states). The asymmetric nature of the signal with respect to the E_F is characteristic of nonequilibrium carrier excitation and subsequent relaxation, consistent with the formation of a transient hot-electron distribution. We note that the depletion appears longer lived than the filling. A plausible interpretation is that the positive signal tracks the rapid decay of the hottest carriers, while the negative response may additionally include the contribution of a small pump-induced spectral shifts or line-shape distortions that relaxes more slowly than the hot-electron population [45]. However, resolving this quantitatively would require a wider delay window and a more detailed multi-component analysis, which is beyond the scope of the present work.

A quantitative assessment of the transient electronic response is obtained from photoemission spectra in the vicinity of E_F, as shown in Fig. 3a for selected pump-probe delays. The spectra are fitted using a Fermi-Dirac distribution convoluted with a Gaussian function, which accounts for the finite experimental energy resolution (around 120 meV FWHM). This approach provides a description of the transient occupied electronic distribution and allows us to extract effective quasi-thermal electronic temperature $T_e(t)$ from the Fermi-edge broadening [46]. Because the temporal resolution of the experiment is 110 fs, possible non-thermal contributions at the earliest pump-probe delays cannot be fully resolved. Accordingly, the extracted T_e should be interpreted as an effective electronic temperature: its rise reflects pump-induced electronic heating, while the subsequent decay describes cooling of an approximately thermalized electronic distribution. For completeness, the full fit model and the associated fit parameters are provided in the Supplementary information.

We then plot the temperature change $\Delta T_e(t) = T_e(t) - T_{e0}$ (where T_{e0}

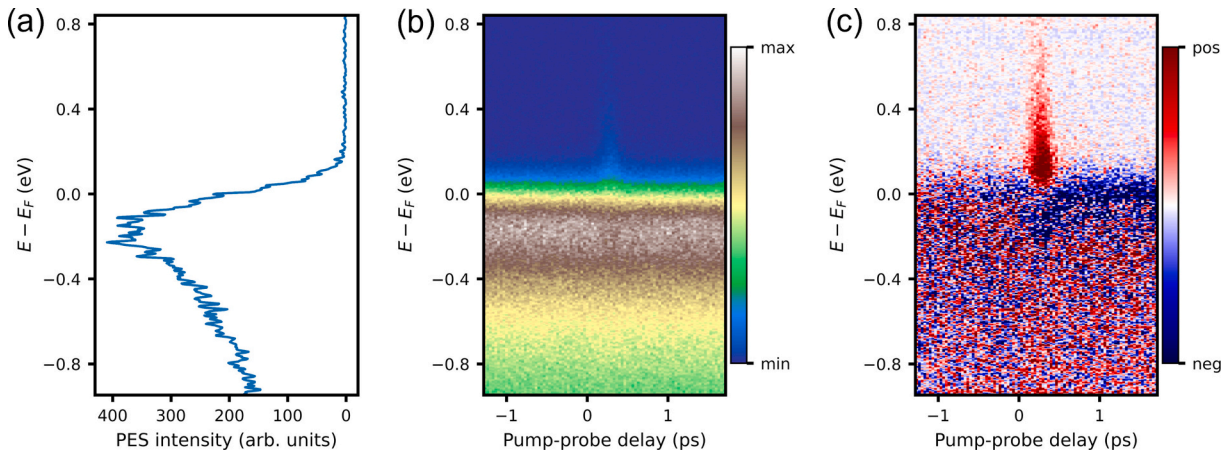

Fig. 2. (a) Photoemission energy distribution curve (EDC) of the $Ti_3C_2T_x$ thin film recorded without optical excitation, plotted as a function of energy referenced to the Fermi level ($E - E_F$). (b) Time-resolved photoemission intensity map versus pump–probe delay, showing the pump-induced redistribution of spectral weight near E_F. (c) Differential photoemission map obtained by subtracting the equilibrium spectrum at negative delays, highlighting transient gain (red) and loss (blue) features. The data reveal ultrafast excitation followed by sub-picosecond relaxation of hot electrons.

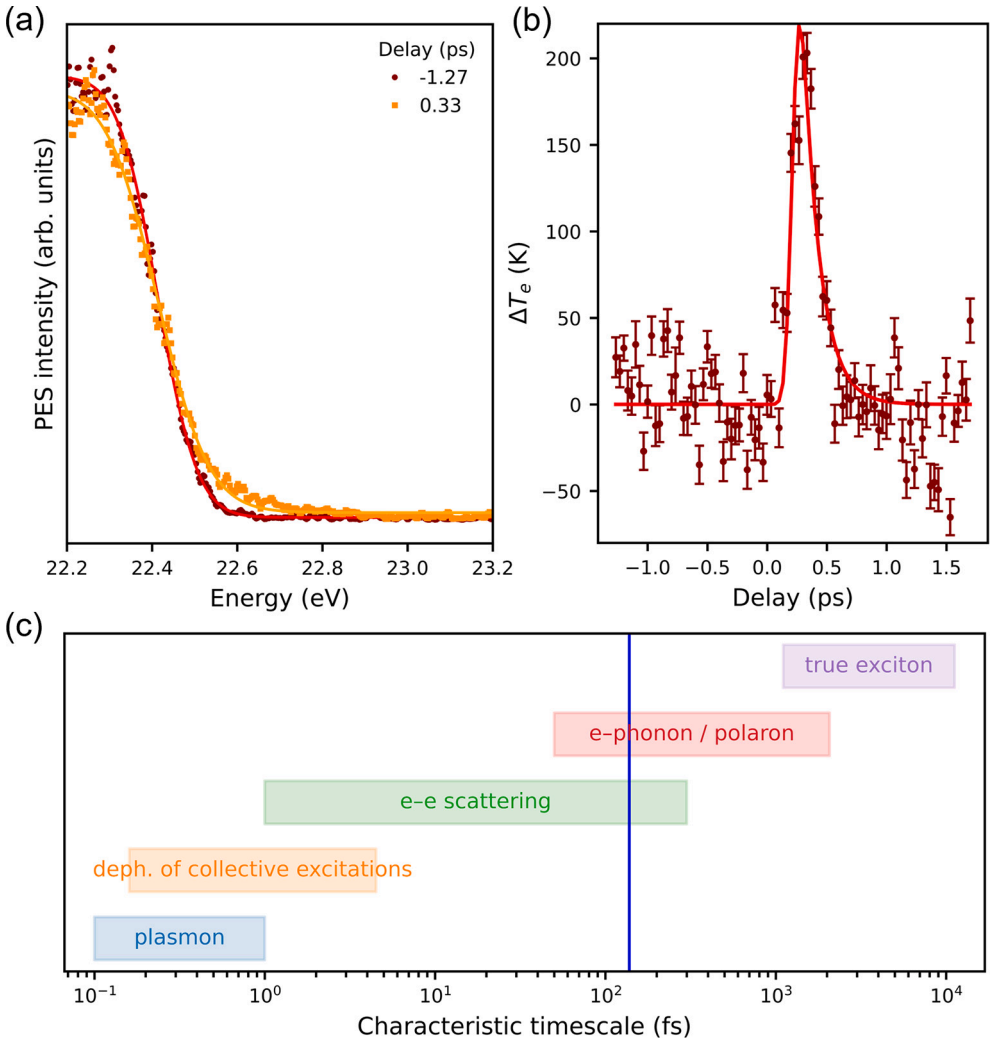

Fig. 3. (a) Photoemission spectra (shown as points) around the Fermi level taken at different temporal intervals of the pump-probe delay and fitted with a Fermi-Dirac distribution convoluted with a Gaussian function, shown as solid line. (b) The extracted electron temperature change (ΔT_e) as a function of pump-probe delays with the corresponding fit from Eq. (1) (red line). (c) Overview of timescales for characteristic ultrafast processes in solids adapted from [47]. This figure includes plasmon dynamics, dephasing of collective excitations, electron-electron scattering, electron-phonon/polaron relaxation and true-exciton processes. The vertical blue line represents relaxation time extracted from the fit.

is the average electronic temperature extracted at negative delays from the same analysis - see Supplementary information), as a function of pump time delay (displayed in Fig. 3b). This pump-induced temperature change is a reliable quantity describing the heating and cooling of the electron system. Because the observed dynamics approach the experimental time resolution (110 fs), we model the T_e evolution with an instantaneous rise followed by an exponential decay, convoluted with a Gaussian instrument response representing the resolution of the setup:

$$\Delta T_{e,\mathrm{meas}}(t) = B\left[H(t-t_0)e^{-(t-t_0)/\tau_E} \otimes \mathrm{IRF}(t)\right]. \quad (1)$$

The measured electronic temperature $\Delta T_{\mathrm{e,meas}}(t)$ models the pump-induced change in electronic temperature as an exponential relaxation that starts at the pump arrival time t_0, enforced by a Heaviside step function $H(t - t_0)$. The intrinsic response is convolved with a Gaussian instrument response function IRF(t) to account for the finite pump–probe time resolution. The fit parameters B and τ_E describe the amplitude of heating and the characteristic relaxation time, respectively. Its quality was evaluated by inspecting the residuals (shown in the Fig. S4, Supplementary information).

From this analysis and within the experimental time resolution, the electronic response exhibits a fast rise that reaches its maximum within ~200 fs (from onset to peak). Following excitation, the electronic temperature decays with a characteristic time of $\tau_E = 138$ fs, indicating rapid energy dissipation of the photoexcited carriers. The maximum electronic temperature reached after excitation corresponds to a transient temperature increase of about 220 K relative to the baseline. Interestingly, the electronic temperature does not fully return to the initial pre-pump baseline within the measured window.

3.3. Phonon-assisted relaxation pathways

Placing the extracted relaxation timescale into a broader physical context, Fig. 3c summarizes the characteristic temporal regimes associated with different ultrafast excitation and relaxation processes in solids [47]. The blue line is the experimentally determined decay time. Our sub-ps response falls within the electronic thermalization and cooling window: the initial rapid rise is consistent with electron-electron scattering that establishes a hot Fermi-Dirac distribution, while the subsequent exponential decay reflects energy transfer from hot electrons to the lattice via electron-phonon coupling.

To aid the microscopic interpretation of the extracted relaxation time, Fig. 4a schematically summarizes the sequence of elementary processes involved. First, an absorption of the 800 nm pump photon by the electron produces a non-equilibrium electronic distribution. This is followed by a rapid electron-electron scattering regime, mediated by the screened Coulomb interaction, which efficiently redistributes energy within the electronic subsystem and establishes a hot Fermi–Dirac distribution. The subsequent decay of the electronic temperature observed here is instead attributed to energy transfer from the hot electrons to the lattice, governed primarily by electron-phonon scattering, i.e. a hot

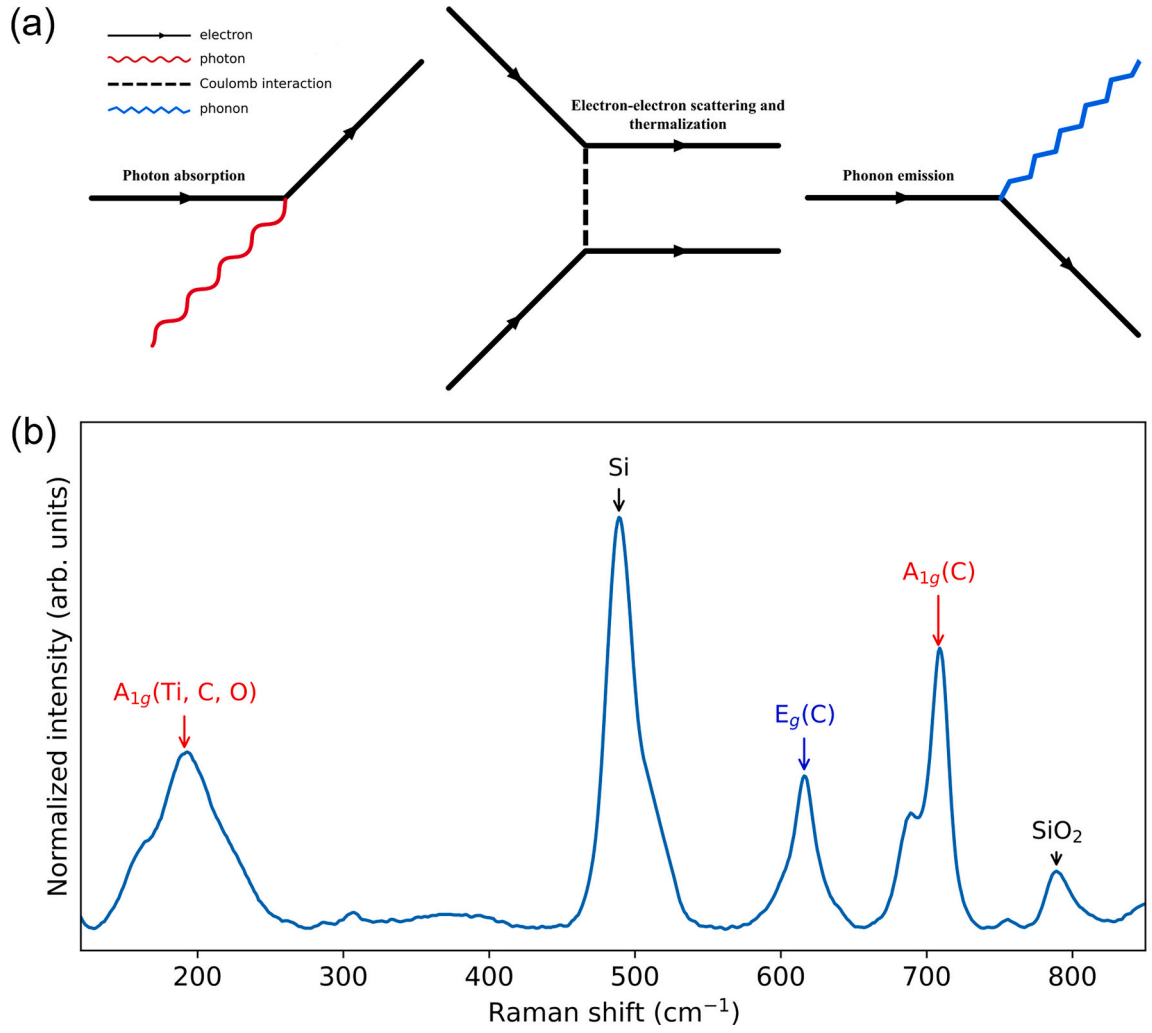

Fig. 4. Graphical illustration of the (a) electron-photon absorption, thermalization via the electron-electron scattering and electron-phonon relaxation process. (b) Raman spectra of the MXene thin film.

electron relaxes by emitting a phonon and scattering into a lower energetic state. More generally, hot carriers with sufficient excess energy can relax efficiently via optical-phonon emission, which commonly provides a fast initial energy-loss channel [48].

Beyond describing relaxation as a sequence of individual scattering events, electron-phonon interactions can also be viewed in terms of polaron formation, where a conduction electron becomes dressed by a surrounding lattice distortion. In $Ti_3C_2T_x$, this behaviour has been discussed in terms of coupling to optical phonons, with reported momentum scattering times (τ_m) on the order below 70 fs at room temperature [29]. While τ_m characterizes momentum relaxation, its magnitude provides a useful yardstick: $\tau_E \approx 138$ fs corresponds to around two momentum-scattering times ($\tau_E/\tau_m \approx 2$), consistent with very efficient electron-to-lattice energy transfer. Comparable sub-200-fs carrier–phonon relaxation has been reported in ultrafast transient-absorption measurements, which yield a room-temperature carrier–-phonon coupling time constant τ_{e-ph} of 115 fs [28].

To this end, we consider the Raman-active optical phonon modes of $Ti_3C_2T_x$ and their characteristic energies. Raman spectroscopy (Fig. 4b), which probes zone-centre phonons, reveals three $Ti_3C_2T_x$ peaks at approximately 191, 616 and 708 cm^{-1}. The peak at 708 cm^{-1} is assigned to the A_{1g}(C) mode and is dominated by carbon vibrations, while the band near 191 cm^{-1} corresponds to the A_{1g}(Ti, C, O) mode [49]. The feature at 616 cm^{-1} is assigned to the E_g(C) mode [50]. In addition, the peaks near 500 and 780 cm^{-1} are attributed to the Si substrate and SiO_2, respectively.

Table 1 summarizes the experimental parameters extracted from the Raman spectra. The phonon modes correspond to emitted phonon energies (E_{ph}) of 23.6, 76.4 and 87.78 meV, respectively. Whether these modes act as an efficient cooling channel depends not only on their energies, but also on their thermal population, which sets the balance between phonon emission (cooling) and absorption (re-heating). The relative likelihood of phonon absorption versus emission is governed by the Bose occupation $N(E_{ph})$

$$N(E_{ph}) = \frac{1}{\exp(E_{ph}/k_B T_l) - 1}, \tag{2}$$

where T_l is the lattice (phonon) temperature. For electron–phonon scattering, the elementary phase-space factors scale as $W_{em} \propto (N+1)$ for phonon emission and $W_{abs} \propto N$ for absorption, giving [51,52].

$$\frac{W_{abs}}{W_{em}} = \frac{N}{N+1} = \exp(-E_{ph}/k_B T_l). \tag{3}$$

At $T = 300$ K, this yields $W_{abs}/W_{em} \approx 3.4 \times 10^{-2}$ for the 708 cm^{-1} mode, i.e. the phonon absorption is only about 3.4% as likely as phonon emission. The corresponding values are 5.2×10^{-2} (5.2%) for the 616 cm^{-1} and 4.0×10^{-1} (40%) for the 191 cm^{-1} mode. Thus, cooling via phonon emission is strongly favoured for the high-energy mode, while the lower-energy mode remains more thermally populated and can exhibit appreciable absorption. Under these conditions, the highest-energy optical phonon provides an efficient cooling channel, since the emission of one to two such phonons per hot carrier is sufficient to remove about 87 to 174 meV.

Comparing this to the characteristic thermal energy $k_B T_e$ (Fermi-Dirac broadening) of the electronic distribution, the range 300–525 K corresponds to 26–45 meV. Therefore, emission of only a few optical phonons is consistent with efficient phonon-mediated cooling. It should be emphasized that the present tr-PES analysis constrains the net electronic cooling rate, not the energy exchanged in individual scattering events. Hence, the "few-phonon" estimate should be viewed as an order-of-magnitude consistency check rather than a direct experimental determination.

Table 1
Experimental Raman bands of the $Ti_3C_2T_x$ MXene thin film, with frequency, phonon energy, mode assignment, spectral origin and the phonon absorption-to-emission ratio.

Raman shift (cm^{-1})	Frequency (THz)	Phonon energy (meV)	Assignment [source]	Absorption relative to emission (W_{abs}/W_{em}) at 300 K
191	5.73	23.68	A_{1g}(Ti, C, O) [49]	4×10^{-1} (40%)
616	18.47	76.37	E_g(C) [50]	5.2×10^{-2} (5.2%)
708	21.23	87.78	A_{1g}(C) [49]	3.4×10^{-2} (3.4%)

4. Conclusion

In conclusion, this time-resolved experimental investigation reveals that photoexcited carriers in a $Ti_3C_2T_x$ thin film relax on a sub-150 fs timescale at room temperature, demonstrating highly efficient electronic cooling. Given the proximity of the transient response to the experimental time resolution, the precise fitted decay time carries some model dependence and should be understood as a characteristic timescale of the relaxation rather than an exact absolute value. Unlike transient optical absorption, which measures changes in the optical response, pump-probe photoemission probes the transient occupied electronic distribution via emitted electrons. This enables a direct determination of electronic heating and cooling from the time-dependent photoelectron energy distribution, while reducing sensitivity to thin-film optical artifacts. Such observed ultrafast cooling points to highly efficient carrier scattering with optical phonons as the dominant energy-loss channel. A direct consequence is that hot, non-thermal carriers decay on an ultrafast timescale of a few hundred femtoseconds or less, so longer-time dynamics reflect near-thermal electrons and heat flow. The reported cooling should therefore be understood as characteristic of the annealed, in situ cleaned $Ti_3C_2T_x$ surface state under ultra-high vacuum conditions and for the specific pump fluence and room-temperature conditions. Such microscopic understanding can guide the optimization of MXene-based optoelectronic and electronic devices, where carrier cooling and electron-phonon scattering directly impact mobility and switching speed. More broadly, the extracted cooling parameters provide a quantitative standard of comparison for modelling the ultrafast energy flow in MXenes.

CRediT authorship contribution statement

Jurij Urbančič: Writing – original draft, Visualization, Project administration, Investigation, Formal analysis, Data curation, Conceptualization. **Fyodor Malchik:** Writing – review & editing, Resources. **Kaiyrgali Zhumadil:** Resources. **Gian Marco Pierantozzi:** Writing – review & editing, Investigation, Data curation. **Monika Schied:** Writing – review & editing, Investigation. **Sara Dottorini:** Investigation. **Riccardo Cucini:** Writing – review & editing, Investigation. **Pietro Parisse:** Writing – review & editing, Investigation. **Giorgio Rossi:** Investigation. **Rokaya Osama:** Investigation. **Lakshmi Rajan:** Investigation. **Egon Pavlica:** Supervision, Resources. **Barbara Ressel:** Supervision.

Declaration of competing interest

The authors declare that they have no known competing financial interests or personal relationships that could have appeared to influence the work reported in this paper.

Acknowledgments

We acknowledge the financial support from the Slovenian Research and Innovation Agency (ARIS) under research core funding No. P1-0055 and project (Gravitacija, GC-0003). This project has received funding from the European Union's Horizon 2020 - Research and Innovation

Framework Programme, under grant agreement No 101007417 NFFA-Europe Pilot.

Appendix A. Supplementary data

Supplementary data to this article can be found online at https://doi.org/10.1016/j.diamond.2026.113690.

Data availability

Data will be made available on request.

References

[1] F. Schmitt, et al., Transient electronic structure and melting of a charge density wave in TbTe3, Science 321 (5896) (2008) 1649–1652.
[2] U. Bovensiepen, P.S. Kirchmann, Elementary relaxation processes investigated by femtosecond photoelectron spectroscopy of two-dimensional materials, Laser Photonics Rev. 6 (5) (2012) 589–606.
[3] R. Cortés, et al., Momentum-resolved ultrafast electron dynamics in superconducting Bi 2 Sr 2 CaCu 2 O 8+ δ, Phys. Rev. Lett. 107 (9) (2011) 097002.
[4] L. Rettig, et al., Ultrafast momentum-dependent response of electrons in antiferromagnetic EuFe 2 As 2 driven by optical excitation, Phys. Rev. Lett. 108 (9) (2012) 097002.
[5] C.L. Smallwood, et al., Tracking Cooper pairs in a cuprate superconductor by ultrafast angle-resolved photoemission, Science 336 (6085) (2012) 1137–1139.
[6] S. Mathias, et al., Self-amplified photo-induced gap quenching in a correlated electron material, Nat. Commun. 7 (1) (2016) 12902.
[7] A. McPherson, et al., Studies of multiphoton production of vacuum-ultraviolet radiation in the rare gases, J. Opt. Soc. Am. B 4 (4) (1987) 595–601.
[8] M. Ferray, et al., Multiple-harmonic conversion of 1064 nm radiation in rare gases, J. Phys. B Atomic Mol. Phys. 21 (3) (1988) L31.
[9] R. Haight, J. Silberman, Surface intervalley scattering on GaAs (110): direct observation with picosecond laser photoemission, Phys. Rev. Lett. 62 (7) (1989) 815.
[10] F. Meier, et al., Time-resolved photoemission spectroscopy on ferromagnetic surfaces and thin films, J. Magn. Magn. Mater. 93 (1991) 523–528.
[11] E.A. Gibson, et al., Coherent soft x-ray generation in the water window with quasi-phase matching, Science 302 (5642) (2003) 95–98.
[12] E.J. Takahashi, T. Kanai, K. Midorikawa, High-order harmonic generation by an ultrafast infrared pulse, Appl. Phys. B 100 (1) (2010) 29–41.
[13] E.J. Takahashi, et al., Coherent water window X ray by phase-matched high-order harmonic generation in neutral media, Phys. Rev. Lett. 101 (25) (2008) 253901.
[14] T. Suzuki, S. Shin, K. Okazaki, HHG-laser-based time- and angle-resolved photoemission spectroscopy of quantum materials, J. Electron Spectrosc. Relat. Phenom. 251 (2021) 147105.
[15] T. Rohwer, et al., Collapse of long-range charge order tracked by time-resolved photoemission at high momenta, Nature 471 (7339) (2011) 490–493.
[16] J.C. Petersen, et al., Clocking the melting transition of charge and lattice order in 1 T-TaS 2 with ultrafast extreme-ultraviolet angle-resolved photoemission spectroscopy, Phys. Rev. Lett. 107 (17) (2011) 177402.
[17] G. Adhikary, et al., Orbital-dependent electron dynamics in Fe-pnictide superconductors, Phys. Rev. B 98 (20) (2018) 205142.
[18] J.-J. Song, et al., Unveiling the 5f electron hybridization process in the antiferromagnetic heavy-fermion superconductor UPd2Al3 via ARPES and time-resolved PES, Fundam. Res. (2025).
[19] J.C. Johannsen, et al., Direct view of hot carrier dynamics in graphene, Phys. Rev. Lett. 111 (2) (2013) 027403.
[20] I. Gierz, et al., Snapshots of non-equilibrium Dirac carrier distributions in graphene, Nat. Mater. 12 (12) (2013) 1119–1124.
[21] H. Shi, et al., Ambient-stable two-dimensional titanium carbide (MXene) enabled by iodine etching, Angew. Chem. Int. Ed. 60 (16) (2021) 8689–8693.
[22] M. Naguib, et al., Two-dimensional nanocrystals: two-dimensional nanocrystals produced by exfoliation of Ti3AlC2 (Adv. Mater. 37/2011), Adv. Mater. 23 (37) (2011) 4207.
[23] S. Ahmad, et al., An overview of recent advances in the synthesis and applications of the transition metal carbide nanomaterials, Nanomaterials 11 (3) (2021) 776.
[24] Y. Gogotsi, B. Anasori, The rise of MXenes, in: MXenes, Jenny Stanford Publishing, 2023, pp. 3–11.
[25] A.S. Zeraati, et al., Improved synthesis of Ti 3 C 2 T x MXenes resulting in exceptional electrical conductivity, high synthesis yield, and enhanced capacitance, Nanoscale 13 (6) (2021) 3572–3580.
[26] J. Urbančič, et al., Time-of-flight photoconductivity investigation of high charge carrier mobility in Ti3C2Tx MXenes thin-film, Diam. Relat. Mater. 135 (2023) 109879.
[27] A. Rawat, et al., Investigation of charge carrier dynamics in a Ti3C2Tx MXene for ultrafast photonics applications, Mater. Adv. 4 (23) (2023) 6427–6438.
[28] J. Zhao, et al., Evidence of surface-mediated carrier-phonon scattering in MXene, ACS Nano 17 (23) (2023) 23714–23722.
[29] W. Zheng, et al., Band transport by large Fröhlich polarons in MXenes, Nat. Phys. 18 (5) (2022) 544–550.
[30] E. Colin-Ulloa, et al., Ultrafast spectroscopy of plasmons and free carriers in 2D MXenes, Adv. Mater. 35 (8) (2023) 2208659.
[31] Q. Zhang, et al., Simultaneous capturing phonon and electron dynamics in MXenes, Nat. Commun. 13 (1) (2022) 7900.
[32] R. Osama, et al., Aging effect on Ti3C2Tx MXene: a morphological, electronic, and electrical investigation, Phys. Status Solidi (RRL) Rapid Res. Lett. 20 (2) (2025) e202500372.
[33] A. Lee, et al., Multi-year study of environmental stability of Ti3C2T x MXene films, Graphene 2D Mater. 9 (1) (2024) 77–85.
[34] R. Cucini, et al., Coherent narrowband light source for ultrafast photoelectron spectroscopy in the 17–31 eV photon energy range, Struct. Dyn. 7 (1) (2020).
[35] NFFA-Europe, NFFA-SPRINT facility @ CNR-IOM, Available from: https://nffa.eu/offer/area/technique/?id=6340, 30 January 2026.
[36] S. Eich, et al., Time-and angle-resolved photoemission spectroscopy with optimized high-harmonic pulses using frequency-doubled Ti: sapphire lasers, J. Electron Spectrosc. Relat. Phenom. 195 (2014) 231–236.
[37] L. Wang, et al., Synthesis and electrochemical performance of Ti3C2Tx with hydrothermal process, Electron. Mater. Lett. 12 (5) (2016) 702–710.
[38] A. Feng, et al., Two-dimensional MXene Ti3C2 produced by exfoliation of Ti3AlC2, Mater. Des. 114 (2017) 161–166.
[39] X. Wang, et al., Large-size Ti3C2Tx microsheets for lightweight and wide-frequency microwave absorption, J. Mater. Sci. Mater. Electron. 33 (26) (2022) 21091–21100.
[40] J.L. Hart, et al., Control of MXenes' electronic properties through termination and intercalation, Nat. Commun. 10 (1) (2019) 522.
[41] M. Schied, et al., Reactivity of Ti3C2Tx MXene with atomic hydrogen: tuning of surface terminations by halogen removal and reversible O to OH conversion, Chem. Mater. 36 (24) (2024) 11905–11919.
[42] L.-Å. Näslund, et al., Chemical bonding of termination species in 2D carbides investigated through valence band UPS/XPS of Ti3C2Tx MXene, 2D Mater. 8 (4) (2021) 045026.
[43] Y. Wang, et al., MXene-modulated electrode/SnO2 interface boosting charge transport in perovskite solar cells, ACS Appl. Mater. Interfaces 12 (48) (2020) 53973–53983.
[44] T. Schultz, et al., Surface termination dependent work function and electronic properties of Ti3C2Tx MXene, Chem. Mater. 31 (17) (2019) 6590–6597.
[45] S. Ulstrup, et al., Ramifications of optical pumping on the interpretation of time-resolved photoemission experiments on graphene, J. Electron Spectrosc. Relat. Phenom. 200 (2015) 340–346.
[46] J. Kröger, et al., The photoemission Fermi edge as a sample thermometer? J. Electron Spectrosc. Relat. Phenom. 113 (2) (2001) 241–251.
[47] H. Petek, S. Ogawa, Femtosecond time-resolved two-photon photoemission studies of electron dynamics in metals, Prog. Surf. Sci. 56 (4) (1997) 239–310.
[48] M. Massicotte, et al., Hot carriers in graphene – fundamentals and applications, Nanoscale 13 (18) (2021) 8376–8411.
[49] A. Sarycheva, Y. Gogotsi, Raman spectroscopy analysis of the structure and surface chemistry of Ti3C2Tx MXene, Chem. Mater. 32 (8) (2020) 3480–3488.
[50] E. Berger, Z.-P. Lv, H.-P. Komsa, Raman spectra of 2D titanium carbide MXene from machine-learning force field molecular dynamics, J. Mater. Chem. C 11 (4) (2023) 1311–1319.
[51] C. Trallero Giner, I.G. Lang, S.T. Pavlov, Theory of multiphonon resonance Raman scattering as a function of temperature in polar semiconductors, Phys. Status Solidi B 106 (1) (1981) 349–357.
[52] B.K. Ridley, W.J. Schaff, L.F. Eastman, Hot-phonon-induced velocity saturation in GaN, J. Appl. Phys. 96 (3) (2004) 1499–1502.